Surface & Coatings Technology 452 (2023) 129068

Contents lists available at ScienceDirect

Surface & Coatings Technology

journal homepage: www.elsevier.com/locate/surfcoat

Integrity of APS, HVOF and HVAF sprayed NiCr and NiCrBSi coatings based on the tensile stress-strain response

Tommi Varis [a,*], Aki Mäkelä [b], Tomi Suhonen [c], Jussi Laurila [a], Petri Vuoristo [a]

[a] Tampere University, Faculty of Engineering and Natural Sciences, Tampere, Finland
[b] Aurubis Finland Oy, Pori, Finland
[c] VTT Technical Research Centre of Finland Ltd, Espoo, Finland

ARTICLE INFO

Keywords:
Micro-tensile testing
Lamella cohesion
Thermal spray coatings
HVAF
HVOF
APS
Cavitation erosion
Fracture surface
Fracture strength
Self-fluxing alloy

ABSTRACT

The interlamellar cohesion of thermal spray coatings influences greatly their mechanical properties and ability to use coatings in different loading conditions and wear/erosion resistance. In the present study, micro-tensile testing of free-standing coatings was utilized to evaluate the mechanical response of thermally sprayed coatings. In addition, the longitudinal uniaxial fracture strength of free-standing coatings could be determined by a tensile test. The coating materials studied were NiCr and NiCrBSi coatings sprayed by atmospheric plasma spraying (APS), high velocity oxy-fuel (HVOF), and high velocity air-fuel (HVAF) processes. The different materials used for the coatings sprayed by different methods yield different microstructures, different stress-strain relation in tensile testing. Different tensile test response was found to be related to cohesion strength between lamellas, and thus was affecting the cavitation erosion wear. The effect of other factors such as hardness and residual stresses on cavitation resistance were also discussed. Such results are crucial to understand the suitability of microstructures obtained by TS processes for different wear conditions.

1. Introduction

Thermally sprayed coatings are formed in a process in which a fully or partially melted particles strike and solidify on a substrate or previously sprayed layer. Particles are attached by mechanical, chemical, and physical (van der Waals) bonds [1–3]. The cohesion between these so-called lamellae greatly influences the mechanical properties of the coating. It has been estimated that depending on the spraying method the degree of cohesion between the lamellae is only 20–80 % of the surface area of the lamella boundaries [4]. In many cases, the limited lamellar cohesion or lack of cohesive areas prevents the good mechanical and wear properties of the actual coating material from being exploited in many applications, especially where high load bearing capacity is required [5,6]. It is understood, that due to the nature of the thermal spray process the mechanical properties of thermally sprayed coatings are worse than those of corresponding solid materials and the properties are anisotropic, i.e., they depend on the load direction. These are attributed to the low interlamellar splat cohesion, interlamellar porosity/microcracks, shape of the lamella, and residual stresses [7–9]. For metallic coatings oxidation of the splats affects the properties of the lamella boundaries as well. Therefore, elastic modulus determinations using methods where the stress field crosses several lamellar boundaries produce a lower modulus of elasticity than what an internal modulus of elasticity based on deformation of the intrinsic material would be [6,7,10–13].

The interlamellar cohesion of the coating is affected by many processing related factors, such as the velocity and temperature of the particles, the temperature of the part to be coated and the powder manufacturing technology used [10,14]. Since different processes produce different splat temperatures and velocities, not only are the shape and amount of the pores and oxides formed in the coating varies, but also different processes flatten the splats differently and thus the cracks at the lamellar boundaries and the orientation of the pores and cracks vary between processes. This is of great importance for the mechanical properties [12]. In the case of very flat splats, the length of the continuous lamellar edges perpendicular to the coating is considerably greater than their length parallel to the plane of the coating. At lower degrees of flattening, this relationship changes. Consequently, thermally sprayed coatings are anisotropic, with different properties perpendicular to the substrate and along the length of the coating [7,10,15,16]. For these reasons, measurements of mechanical properties by different methods produce different results due to the measurement orientation and force

* Corresponding author.
E-mail address: tommi.varis@tuni.fi (T. Varis).

https://doi.org/10.1016/j.surfcoat.2022.129068
Received 1 August 2022; Received in revised form 30 October 2022; Accepted 9 November 2022
Available online 17 November 2022

[17]. For this reason, there is also no strong correlation between mechanical properties and wear resistance.

As a result of interlamellar defects, thermal sprayed coatings have shown non-linear mechanical response. This means that an increase in stress causes a larger strain than in an ideally elastic material and that elastic modulus is stress dependent [18]. Non-linearity can be due to reversible (elastic) or permanent deformations. Typical permanent deformation of thermally sprayed coating in load is microcracking, which is permanent and remains in the material when stress is released. It should be mentioned that these microcracks can occur at the lamellar boundaries already during the manufacturing process due to the so-called quenching stresses caused by the shrinkage of the splats [8,19]. Non-linear elastic deformations are non-permanent and recover when the stress is released. Recent extensive studies on TBC coatings have demonstrated such a non-linear elastic (anelastic) mechanical response for zirconia coatings [20–23]. Liu et al. [20,23] thermally cycled the coating on the substrate while measuring the deflection and observed an anelastic stress-curvature response and suggested that the nonlinear behaviour of the zirconia coating is due to crack opening and closing and crack surface friction associated with sliding of the crack interface. Dwiwedi et al. [21] used same apparatus as they optimized the thermal conductivity properties of TBC by exploiting the degree of nonlinearity, which correlates well with the porosity of the coating. Non-linear stress-strain -response has also been observed in tensile tests for metallic (NiCr) free standing coatings [24]. For these, the loading and subsequent release of tension produced a permanent elongation, suggesting micro-cracking. *Re*-loading to already loaded level produced an anelastic response, which was similar to that observed for ceramics. In this sense, it is necessary to consider that the quenching of splats generates significant tensile stresses in the coating during the coating process, which may create microcracks at the lamellar boundaries. When externally loaded, micro-cracking may start immediately when an external force is applied to the structure, as demonstrated by acoustic emission studies [25,26].

The direct measurement of the cohesion between lamella is challenging. In the direction of the force perpendicular to the coating and substrate, which determines the adhesion of thermally sprayed coatings is generally measured by standard tests such as ASTM C633–01 (2008) [8] and ISO 14916: 1999241 [9]. In this study, the free-standing thermally sprayed coatings were subjected to a uniaxial stress state by utilizing miniature tensile test in a SEM chamber, which allowed very accurate stress-strain response analysis. To our knowledge this is reportedly the first time this has been done for thermally sprayed coatings. The coating materials studied were NiCr and NiCrBSi coatings sprayed by APS, HVOF and HVAF processes. The different materials used for the coatings sprayed by different methods yield different microstructures, the mechanical behaviour of which will be investigated in a tensile test. The effects of various spraying process and methods, and coating materials on such issues as cohesion strength between lamellas, stress-strain relation, and cracking behaviour under loading were of interest. Microstructural study and cavitation erosion wear test were conducted to evaluate the coatings and to found relationship between coating structure, mechanical response, and its cavitation erosion resistance.

2. Experimental

2.1. Coating manufacturing

Powders used for the experiments were gas atomised Diamalloy 2001 NiCrBSi and water atomised Ni20Cr powders, Metco 43F- NS (for APS) and Metco 43VF-NS (for HVOF and HVAF), from Oerlikon Metco, Switzerland. Metco 43F-NS and 43VF-NS is designed for corrosion resistance, high temperature corrosion resistance, high temperature oxidation resistance and could be used for example as a bond coat for ceramics. Diamalloy 2001 is a self-fluxing alloy, of which the coating can be used both as sprayed and heat-treated condition. In fused condition Diamalloy is designed for fretting wear protection, sliding wear protection, dimensional restoration, solid particle erosion protection. The B and Si alloyed into the powder lower the melting temperature of the alloy, allowing it to be fused by heat treatment at around 993 °C. In addition, Si acts as a deoxidiser, reducing the concentration of oxide lamellae at the interfaces. In this study the coating was used in as-sprayed condition, with the aim of studying the effect of a lower melting point and the deoxidising effect of the alloy on interlamellar adhesion. Composition of powders and their particle sizes are presented in Table 1.

The coatings were prepared by HVAF, HVOF and APS spraying, which achieve very different microstructures. The HVAF gun used was a M3 propane spray gun from Uniquecoat Technologies LLC (Oilville, USA) equipped with a 4 L4 ceramic nozzle. The HVOF gun was an Oerlikon Metco AG Diamond Jet Hybrid 2700 (Wohlen, Switzerland) with air cap 2701 and the APS gun was a ProPlasma HP 6.5 from Saint-Gobain (Avignon, France) connected to Plasma-Technik A3000 operating system (Oerlikon Metco/Plasma-Technik, Switzerland). Powder was fed through a 1.8 mm diameter powder feed nozzle set perpendicularly upwards at a radial distance of 7 mm. Coatings, with thicknesses mentioned in Table 2, were sprayed on 100 × 50 × 5 mm structural steel, which were sandblasted using 500–700 μm corundum sand. Spray parameters are presented in Table 2. For the Saint Gobain Pro plasma (APS), the parameters used for spraying of NiCr and NiCrBSi were those recommended for the NiCr bond coat by the manufacturer of the ProPlasma. For the DJ Hybrid (HVOF) process the air cap 2702 was used with the parameters that were recommended for the air cap. It should be noted that for Diamalloy 2001 powder and NiCr powders, the recommended air cap is 2701. However, previous studies have found that this produces large amounts of non-melted particles in NiCr materials, which are highly undesirable because they adversely affect corrosion resistance [29,30]. Therefore, instead a 2702 air cap was used. In HVAF M3 processes, the bases of the hardware and parameter selection can be found in reference [31]. A ceramic 4L4C nozzle and a ceramic primary nozzle were chosen for the deposition to avoid powder build-up in the nozzles. In addition, a small combustion chamber was used to avoid powder clogging of the combustion chamber. The gun was adjusted close to maximum chamber pressure (approximately 97 % of the maximum), because it is generally known that particle velocity increases with increasing chamber pressure. However, the maximum pressure is limited by the capacity of the air compressor. The fuel/air ratio of the M3 equipment was adjusted to ensure the stable burning of the flame. This adjustment range in the gun is relatively limited since it only works well over a relatively narrow range.

The coatings were applied with a robot using 0.9 m/s traverse speed and a step width of 4 mm. The substrate temperature was monitored during spraying with a Fluke Ti300 (Everett, WA, USA) thermal imager. During spraying, the temperature of the samples was controlled by the length of the waiting time between sweeps. The temperature ranges are shown in Table 2. For two of the NiCrBSi coatings, and two NiCr coatings, (HVOF-C and HVAF-C, the start of the new coating layer was delayed until the surface temperature was around 403 K. These are indicated in the sample name by the letter C (=cold). During the spraying of the layer, the substrate temperature reached a maximum of 458–463 K. The two coatings, HVOF-H and HVAF-H, indicated by letter H, were applied to a hotter substrate by continuously coating 10 passes with a maximum temperature of 573 K. Before the next series of 10 sweeps, the surface temperature was cooled down to 523 K. Finally, the temperature range for APS NiCrBSi and NiCr deposition was 373 K to 423 K.

2.2. Deposition stress measurements

For the deposition stage stress measurements depositions were in situ evaluated by property (ICP) sensor [31] by ReliaCoat Technologies, East

Table 1
Powder compositions and particle sizes. Diamalloy 2001, Metco 43F – NS, and Metco 43VF-NS nominal weight percentages acquired from manufacturer's online resources [27,28].

Powder	Ni	Cr	B	Si	C	Fe	Mn	Others (max)	Particle size (μm)
Diamalloy 2001	Bal.	17	3.5	4	1	4	–	–	15–45
Metco 43F- NS	Bal.	19.5	–	1.2	–	0.25	0.25	0.5	10–63
Metco 43VF-NS	Bal.	19.5	–	1.2	–	0.25	0.25	0.5	5–45

Table 2
Spraying parameters, resulted thickness/pass and substrate temperatures.

		NiCr APS	NiCr HVOF	NiCr HVAF	NiCrBSi APS-C	NiCrBSi HVOF-C	NiCrBSi HVAF-C	NiCrBSi HVOF-H	NiCrBSi HVAF-H
Propane 1 Pressure	MPa	–	–	0.76	–	–	0.76	–	0.76
Propane 2 Pressure	MPa			0.69	–	–	0.69	–	0.69
Air Pressure	MPa	–	–	0.79	–	–	0.79	–	0.79
Propane Flow	$l{\cdot}min^{-1}$	–	70	–	–	70	–	70	–
Oxygen Flow	$l{\cdot}min^{-1}$	–	238	–	–	238	–	238	–
Air Flow	$l{\cdot}min^{-1}$	–	375	–		375	–	375	
Current	A	500	–	–	500	–	–	–	–
Voltage	V	73			71				
Power	W	36.8			35.5				
Argon Flow	$l{\cdot}min^{-1}$	55	–	–	55	–	–	–	–
Hydrogen Flow	$l{\cdot}min^{-1}$	8	–	–	8	–	–	–	–
Carrier Gas Flow	$l{\cdot}min^{-1}$	4	20	60	4	20	60	20	60
Stand-off Distance	m	120	250	300	120	250	300	250	300
Powder feed rate	$g{\cdot}min^{-1}$	43	60	50	45	40	50	40	40
Thickness/pass	μm	12	16	16	15	18	13	16	13.0
Final thickness	μm	185	630	485	445	485	490	560	515
Substrate Temp.	K	373–403	403–458	403–458	383–423	403–458	408–463	523–573	523–543

Setauket, NY, USA, which measures the temperature and curvature of the substrate beam during spraying [32]. From the curvature resulted from spray passes the good approximation of the deposition stresses, either quenching or peening, in the coating can be calculated by Stoney's equation [33]:

$$\sigma_D = \frac{E_s' t_s^2}{6} \frac{d\kappa}{dt_c}$$

where σ_D is the evolving stress of the layer with thickness t_c, which causes a curvature change *of* $d\kappa$. E_s' is the in-plane elastic modulus ($=E_s / (1 - \nu_s)$, where E_s is Young's modulus and ν_s is Poisson's ratio of the substrate), and t_s is the thickness of the substrate.

The coatings for deposition stress evaluation were sprayed with similar parameters than the actual coatings but on S355 low carbon steel flat bars of 228.6 mm in length, 25.4 mm in width, and 5 mm thick.

2.3. Scanning electron microscopy

For structural analysis, cross-sectional specimens of each coating were prepared by cutting with a precision cutter, casting in resin, and grinding and polishing to a surface roughness of 1 μm. Microstructural analysis of the cross-sectional samples was performed using a JEOL JSM-IT500 (Tokyo, Japan) scanning electron microscope (SEM) in back-scattered electron (BSE) mode using a 15 kV acceleration voltage and a working distance of approximately 10 mm. After the tensile testing the fracture surfaces of the miniature tensile specimens were studied using the same SEM.

The tensile samples were examined during mechanical testing by taking SEM images in type II secondary electron (SE2) mode with a Zeiss Ultra Plus Gemini (Carl Zeiss AG, Oberkochen, Germany) field emission scanning electron microscope (FEG-SEM). Acceleration voltage of 10 kV, 60 μm aperture and a working distance of approximately 33 mm were used to take the pictures.

2.4. Tensile testing

Tensile testing of the free-standing coating specimens was performed with a new type of tensile testing method, which was designed and manufactured by VTT. The test uses miniature specimens and a small specimen fixture frame equipped with a very precise pneumatic control unit and displacement measurement sensor, which allows loading of the tensile specimens inside the SEM chamber. A similar method of testing freestanding coatings was not discovered in literature for thermally sprayed coatings. This ultra-small load frame allows samples as small as 39 mm × 5 mm to be imaged during a tensile test. Loading frame and sample dimensions are shown in Fig. 1.

In this study, free-standing coating samples were used, and the method of preparation was as follows [34]. The samples were first cut to the 39 × 5 mm size using a precision cutter. The coating was then separated from the substrate material by first removing most of the substrate by cutting with a precision cutter close to the coating interface and then grinding off the remaining substrate material. The separated coating surfaces were then polished with a 1 μm diamond suspension. The polished samples were finally cut into a tensile specimen shape using a high precision 20 W Light Conversion Pharos (Vilnius, Lithuania) femtosecond laser with a Raylase Superscan V-15 scanner for beam alignment. The final shape and dimensions of the samples are shown in Fig. 1. After laser cutting, the edges of the samples were still slightly rough and could not be smoothed using any method without the risk of damaging the sample. Fig. 2 shows a narrowed section of a laser cut NiCr HVOF specimen demonstrating the roughness of the specimen. The laser-cut sample was at a satisfactory level for the experiment. Due to the low heat input of the laser, no microstructural changes were observed at the edge of the specimen. However, some loose particles were visible at the edge of the sample, which cause stress concentrations during tensile testing and this notch effect decreases the fracture strength of the coating.

The tensile test was performed according to the following procedure: a) the tensile load was increased until a certain amount of displacement was reached, b) once the desired displacement value was reached, the sample was held at constant tension while c) the SEM imaging was performed before proceeding to the next step, d) the process was repeated until the sample broke down. After the test, the actual cross-sectional area of the fracture of the coatings was determined from

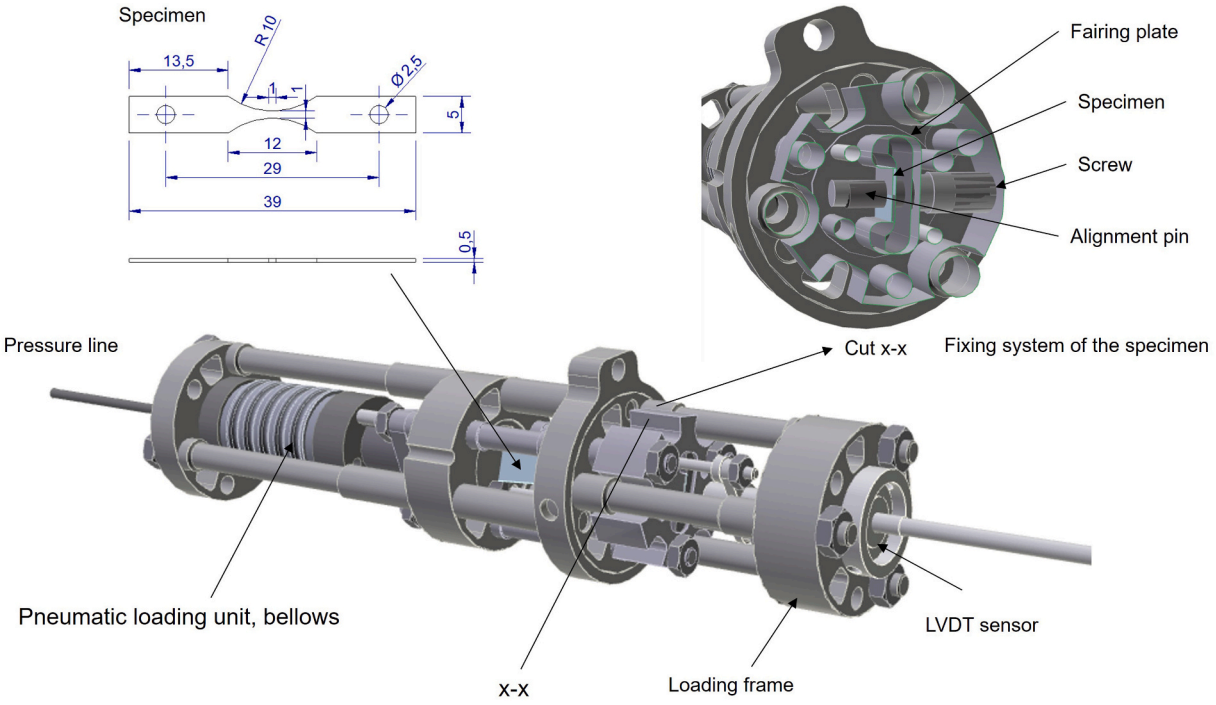

Fig. 1. Tensile testing device with specimen dimensions in mm.

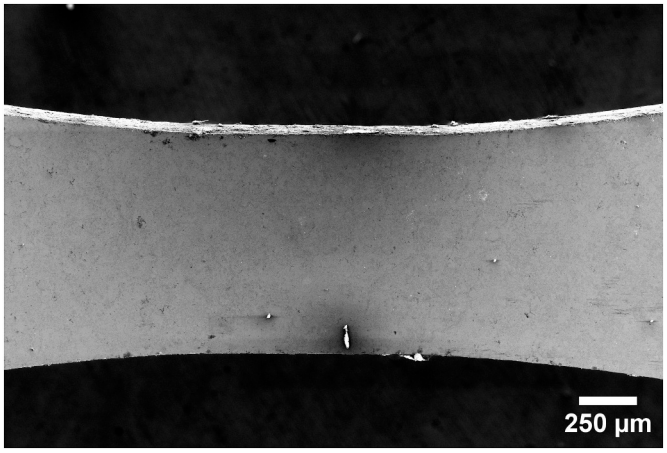

Fig. 2. SEM image of the narrowed part of a laser-cut specimen NiCr HVOF.

sample using SEM.

Typically, a tensile test can be used to determine the modulus of elasticity ($E = \Delta\sigma/\Delta\varepsilon$) of a material. It is the slope of the linear (elastic) part of the stress-strain curve for a material under tension and describes the stiffness of the material. In a tensile test, strain is determined as the relative change in gauge length over the reduced area of the tensile specimen, $\Delta L/L_0$. In our case, due to the small dimensions of the specimen, it was not possible to determine the displacement in the narrowed part of the specimen thus the displacement, ΔL, obtained in our study, was the displacement between the gripping points of the whole specimen including wider part. It was therefore not possible to determine the elastic modulus according to its definition, but instead $\Delta\sigma/\Delta L$ value was used to compare the stiffness of the samples. Value $\Delta\sigma/\Delta L$ describes the specimen stiffness in the same way as the elastic modulus and as the specimen dimensions where this value can be used for comparison of the elastic properties of the samples. It should be noted that the stress, σ, was determined for the narrowed cross section area of the specimens.

The stress that led to the coating fracture can be considered as a fairly good value for the fracture strength in the direction of the coating, but even here one must consider the edge effects caused by the specimen fabrication, such as defects at the edge of the tensile specimen.

2.5. Cavitation testing

Samples were tested according to ASTM G32-16 “Standard Test Method for Cavitation Erosion Using Vibratory Apparatus”. In the test, the test pieces with the size of 25 × 25 × 5 mm, which were ground with 4000 grit abrasive sandpaper were placed in a distilled water and a high-frequency vibrating tip was placed at 500 µm distance from the sample. An ultrasonic transducer VCX-750 from Sonics & Materials, USA, was used for the tests. The vibration caused bubbles to form and collapse in the liquid, and the collapsing bubbles cause damage and erosion (loss of material) of the sample. The vibration tip was an alloy of Ti-6Al-4 V, and tip diameter was 15.9 mm. In the test the frequency was 20 kHz and amplitude 50 µm. Water temperature was kept at 25 °C. The samples were weighed with high accuracy scale after 7.5, 15, 30, 45, and 60 min. Prior to weighing the samples were cleaned in an ultrasonic bath with ethanol and weighed after drying.

3. Results and discussion

3.1. Microstructure and hardness

The microstructures of the cross-sections of the coatings sprayed on colder substrate are shown in Fig. 3. On the left are NiCr coatings and on the right NiCrBSi coatings. The hardness's of the coatings are shown in Table 3.The coatings are a good representation of the typical microstructures obtained by these methods [9,29–31,35,36]. The microstructures of the coatings differ depending on the spraying process used. In the APS-NiCr coating on the top left, the lamellae are very flat and there is a lot of interlamellar porosity between the lamellae. Light grey oxide layers are also visible around the lamellae. The HVOF NiCr coating in the centre left is clearly denser than the APS NiCr coating. The lamellae are also flattened in shape, but the oxides do not appear as ribbons on the edges of the lamellae, but more fragmented. The HVAF

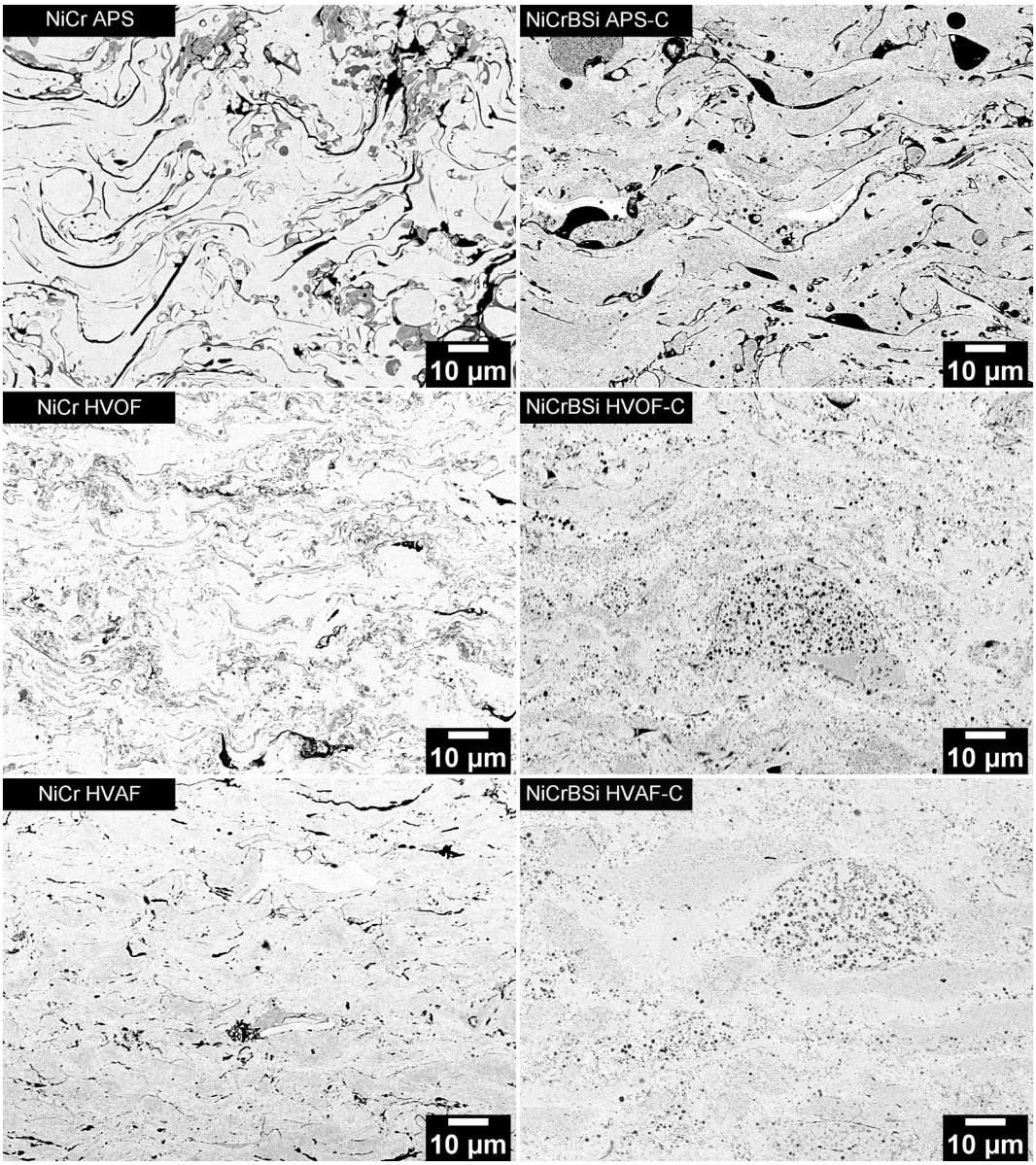

Fig. 3. Cross-sectional back scatter mode SEM images of coatings sprayed on colder substrate (C).

NiCr coating in the bottom left shows hardly any oxides, but there is some porosity due to poor filling, and there is also some porosity between the lamellae. In terms of porosity of NiCrBSi coatings, the APS coating is almost as porous as the NiCr coating, while the HVOF and HVAF NiCrBSi coatings are very dense. In NiCrBi coatings, there appear no lamellae-like or fragmented oxides as in NiCr coatings. One clear difference between hat both HVOF and HVAF NiCrBSi coatings show significantly more non-melted or partially melted (later we will use the term non-melted for both) the size of 30–40 µm particles than the corresponding NiCr coatings sprayed with the same processes. It seems obvious that because the melting point of NiCrBSi is lower, particles of this size achieve a sufficient degree of melting to adhere. NiCr particles of a similar size, on the other hand, do not, but bounce off on impact. The easier adhesion of relatively large particles is further enhanced when the substrate temperature is higher, as will be seen in the later fracture surface images. However, otherwise the microstructures of NiCrBSi coatings sprayed on a hot substrate were not significantly different from those sprayed on a cold substrate. But it should be noted that when depositing on a substrate with a higher temperature (523–573 K), the hardness of the coating increases compared to a coating deposited at lower temperature (403–463).

The other noticeable difference between the microstructures of the NiCrBSi and NiCr coatings is that in the NiCrBSi coatings chromium carbides and chromium borides are present in the Ni matrix [36–38], which clearly increase the hardness of the coatings compared to NiCr. The occurrence and size of these precipitates are affected by the degree of particle melting and are largest in non-melted particles with a structure similar to that of the original powder, where precipitates are already formed during atomization. If the particle is well melted, as can be observed in the APS coating, the size of the precipitates is small because most of them have dissolved in the matrix and have not had time to form an equilibrium structure during rapid cooling.

3.2. Mechanical response of coatings

Fig. 4 shows the stress-displacement curves of the free-standing coatings. In each case, the smoothed curve is plotted on top of the original curve to better illustrate the stress-deformation relationship. The original curve shows an evenly spaced downward spike as the tension is stopped at these points for SEM imaging, which were taken to

Table 3
Hardness, UTS, Δσ/ΔL, cavitation resistance, and deposition stresses of the coatings.

Sample	Deposition stress MPa (-compression)	Hardness HV 0.3 kg	UTS MPa	Δσ/ΔL N/mm^3	Cavitation resistance min/μm
NiCr APS	–	263 ± 27	–	–	5.7
NiCr HVOF	−219	394 ± 11	406	5168	26.1
NiCr HVAF	−433	366 ± 26	597	5986	33.4
NiCrBSi APS-C	432	574 ± 45	533	4011	6.7
NiCrBSi HVOF-C	267	655 ± 94	495	4629	18.7
NiCrBSi HVOF-H	–	742 ± 92	451	4861	26.5
NiCrBSi HVAF-C	−45	715 ± 86	509	6727	41.0
NiCrBSi HVAF-H	–	781 ± 71	377	9773	44.9

look at possible deformations that might be visible in the material. In this case, relaxation occurs in the material and the stress relaxes during the static strain period. It should also be mentioned that, when carried out in this way, the stress level of the curve transmitted by the tension is slightly lower than if the tensile test were carried out continuously.

Fig. 4 shows that, except in three cases, the tensile tests of free-standing coatings were successful. The NiCr APS coating could not be tensile tested because the sample was too fragile to be attached to the test fixture. In specimen NiCrBSi HVOF C, a crack was observed outside the narrowed section, which explains the increase in displacement at a stress level of about 300 MPa. However, it was possible to load more stress into the specimen after the cracking and the final fracture occurred within the narrow section at stress levels above 400 MPa. A discontinuity was also observed in the NiCr HVOF specimen at a stress level of about 230 MPa.

The stress-displacement curves in Fig. 4 show the non-linear stress-displacement behaviour of all coatings. As shown by Liu et al. [20,23], the thermally sprayed material is characterized by non-linear elastic and non-elastic deformations. Non-linear elastic deformations can be thought to be formed in the stressed structure as a result of pore opening and lamellar sliding. These deformations recover when the stress is removed. Inelastic deformations, on the other hand, remain even if the tension is removed and are generated in the coating, e.g. as a result of micro-cracking [39]. By looking at the stress-displacement curves tensile curves in Fig. 4, it is evident that HVAF coating does not undergo as much non-linear or anelastic deformation than HVOF and APS coatings. HVAF coatings have a lower stress-displacement curve slope reduction than APS and HVOF coatings, and it can have argued them to be structurally more solid-like or intact. The HVOF coating is in turn more structurally intact than the APS coating.

In addition to hardness and resistance to cavitation erosion, Table 3 shows Δσ/ΔL and ultimate tensile strength (UTS). The parameter Δσ/ΔL, like the modulus of elasticity, describes the stiffness of the specimen. We have determined the stress-displacement curve Δσ/ΔL value at relatively high stress levels just before fracture, which is shown for the NiCr HVAF specimen in Fig. 4. When comparing the same coating material, it is noticeable that at high stress levels the elastic modulus (or parameter Δσ/Δε) is lower the more non-linear elastic or inelastic deformation occurs in the material. Thus, the parameter Δσ/Δε determined just before the final fracture of the material is thought to be an essential parameter for describing the integrity of the sprayed material, since it includes not only elastic atomic-scale deformations but also non-linear elastic and non-elastic deformations in the coating. The more these non-linear elastic and non-elastic deformations occur in the coating, the more Δσ/ΔL decreases as the loading progresses.

The UTS of NiCr coatings, shown in Table 3, ranged between 406 and 597 MPa. The UTS of NiCrBSi coatings ranged from 377 to 533 MPa. It was noteworthy that for NiCrBSi coatings sprayed on a cold substrate, the best UTS was obtained for the APS sprayed coating and the worst for the HVAF sprayed coating. Furthermore, it should be noted that increasing the substrate temperature did not improve the UTS. However, it should be noted that the surface quality produced by laser cutting is not optimal. It leaves a slight roughness at the edge of the sample due to the detachment of small particles. The notch effect leads to stress concentrations at the edge, which lowers the fracture strength obtained for the coatings. On the other hand, the internal structure of thermally sprayed coatings is in any case rich in defects, which makes UTS a very uncertain quantity due to the random nature of the defects and requires a statistical analysis of several samples to determine it. The impact of defects is further discussed in the fracture surface and analysis in the next section.

3.3. Fracture surface and in-situ SEM observations

The fracture surfaces of the tensile specimens are shown for NiCr in Fig. 5 and for NiCrBSi in Fig. 6. In addition to showing the paths along which the fractures have propagated, the fracture surfaces also provide information on the flattening of the splats and the contact between them. The fracture may have propagated either clearly along the lamellar boundaries or through the particle. In NiCr APS coatings, the fracture surface is not from the tensile test specimen, as the specimen could not be tested at all. Instead, the specimen was fractured by bending to compare its fracture surface with other coatings. The fracture

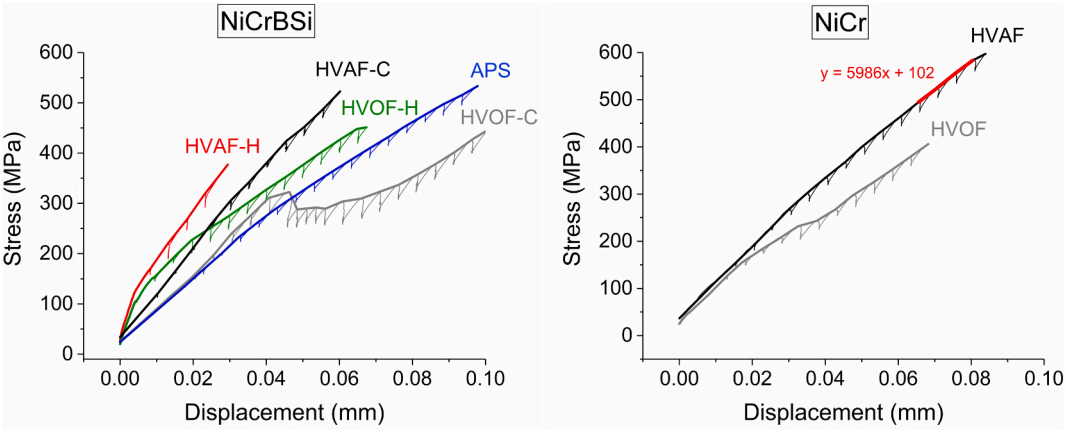

Fig. 4. Stress-displacement curves of the coatings. Fitting of Δσ/Δε shown in curve NiCr HVAF.

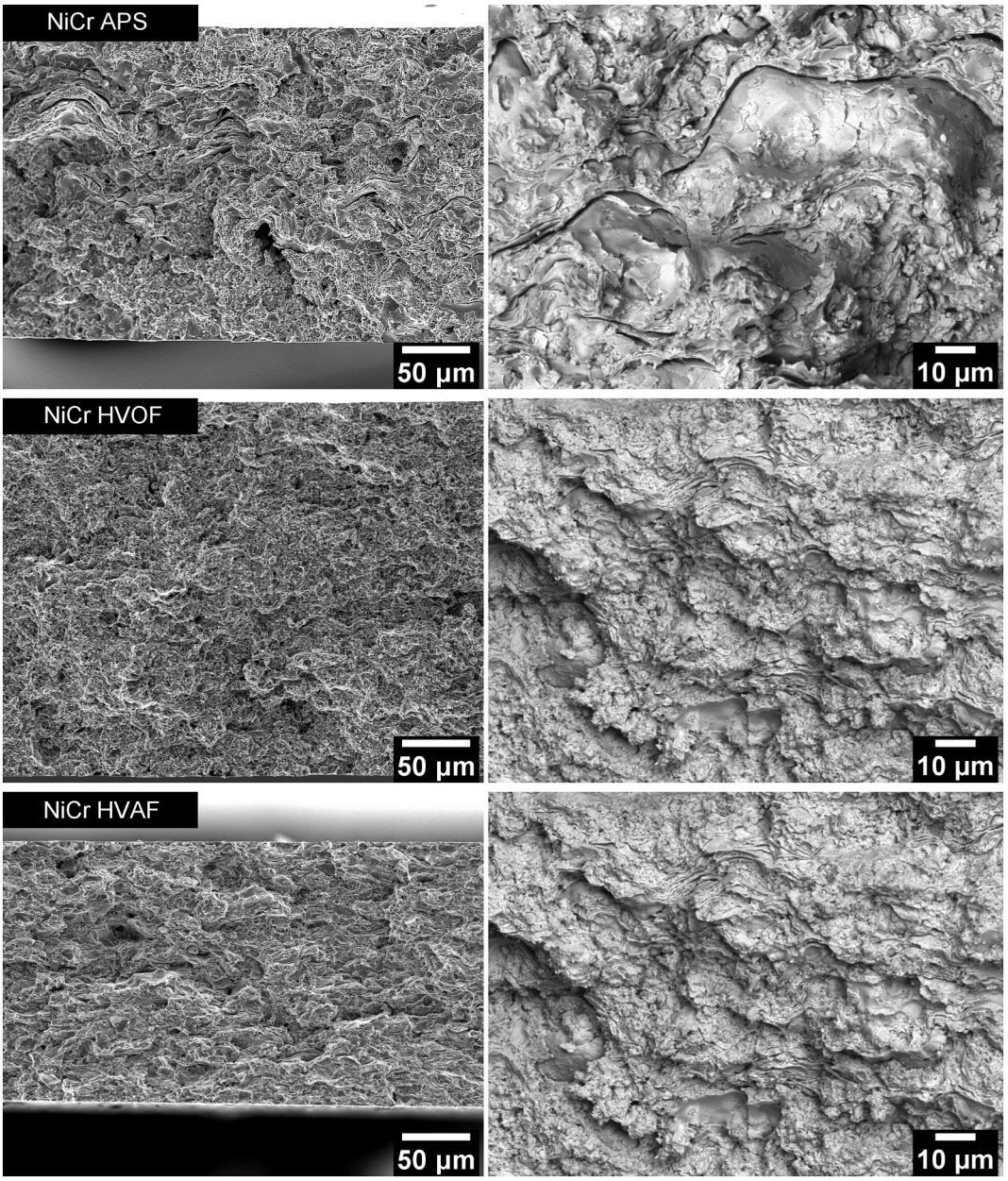

Fig. 5. Fracture surfaces of NiCr coatings by SEM. Lower magnification on the left with scanning electrodes and higher magnification on the right with back scatter detector.

surface of the NiCr APS coating shows well-melted lamellar interfaces with a relatively smooth surface, suggesting that fracture has progressed easily between weak lamellar interfaces. The detached lamellae were also observed in cross-sectional images of APS NiCr coatings, showing poor adhesion. In this coating, where many oxide lamellae are visible in the microstructure, it is likely that the fractures have propagated brittle along the oxide lamellae during the tensile test or have already occurred during cooling and shrinkage of the lamellae. The fracture surfaces of NiCr HVOF and HVAF coatings are similar, with fewer smooth areas than in APS coatings. For most of the cross-sectional surface, the fracture appears to have propagated through the lamella or particle and through lamellae fracture surfaces are rough, indicating a more ductile fracture.

The fracture surface of the NiCrBSi APS coating reveal very strongly flattened lamellae. The flat lamellae of the coatings have fractured through the lamellae and show signs of ductile fracture. There are also some smooth surfaces between the lamellae in the direction of tension, along which the fractured pieces have detached. On the fracture surfaces of NiCrBSi HVOF C and H, the lamellae are not as flattened and the fracture in these has gone through the sprayed particle. These through fractured zones dominate the view. In addition, interlamellar, smooth, detachment surfaces in the direction of tensile strain are seen on NiCrBSi HVOF surfaces. In fracture surfaces of NiCrBSI HVAF C and HVAF H through lamella fractures fracture surfaces are present but also surfaces left by non-melted particles along which the fractures have propagated are observable. A significant number of spherical interfaces non-melted particles are visible on the fracture surface of the HVAF NiCrBSi C and HVAF NiCrBSi H coatings. The HVAF NiCrBSi H coating still has a much higher number of these than the HVAF NiCrBSi C coating. Looking at the UTS of NiCrBSi-C and especially NiCrBSi-H in Table 3, it can be concluded that the non-melted particles remaining in the coating play a key role in the low UTS of these coatings, as the adhesion of the non-melted particles is apparently low.

The coatings were imaged with SEM during the tensile testing. This provided further insight into the behaviour of the coatings under the

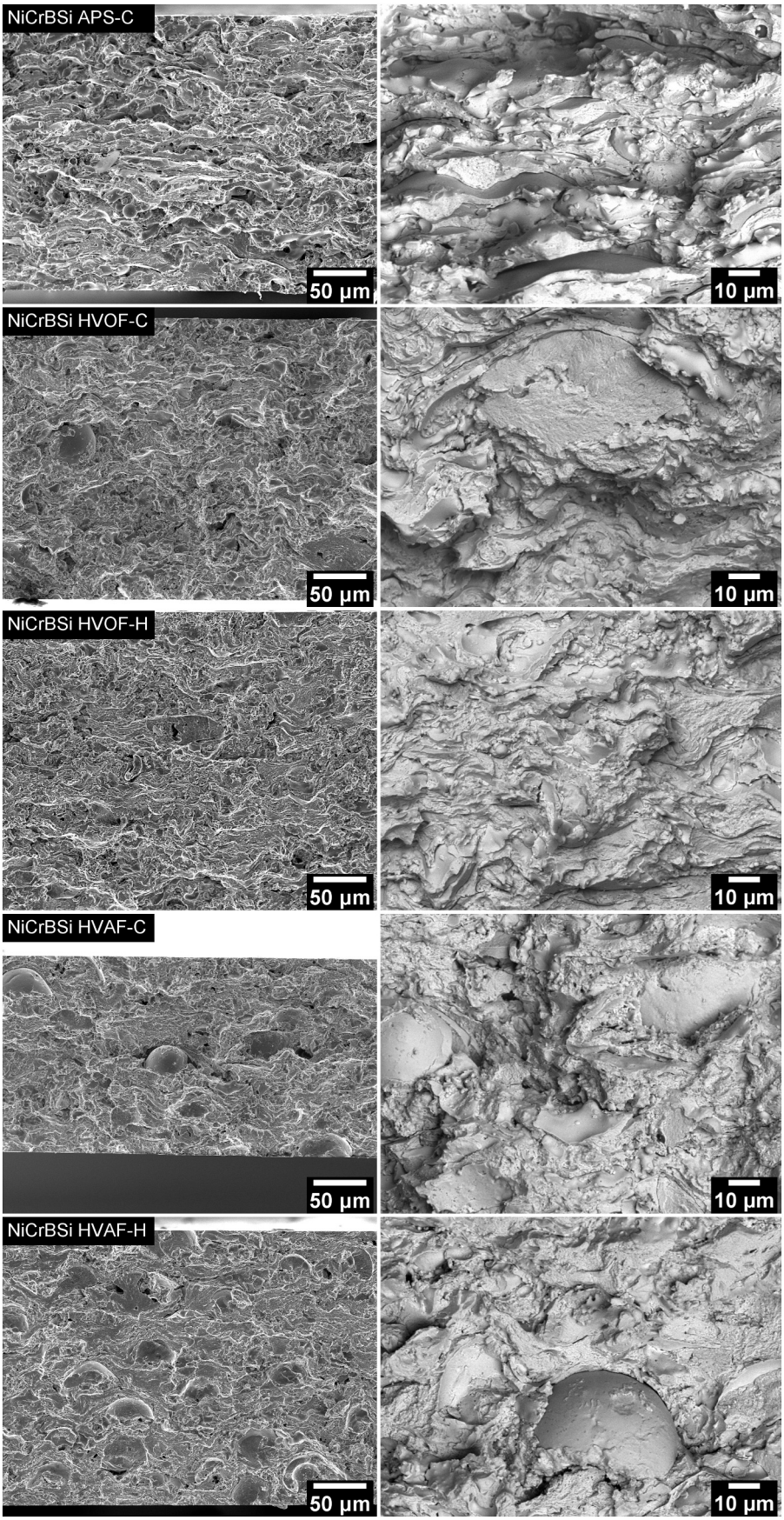

Fig. 6. Fracture surfaces of NiCrBSi coatings by SEM. Lower magnification on the left with scanning electrodes and higher magnification on the right with back scatter detector.

tensile loading. Fig. 7 a and b shows images of the surface of NiCrBSi APS coatings before loading and after 0.094 mm strain. In Fig. 7 b, the coating is stressed to about 500 MPa and cracks or poorly bonded areas on the surface are clearly open. However, the coating has not yet fractured as the well adhered areas of the coating hold the specimen together. Similarly, crack opening of NiCrBSi HVOF C coating is seen in Fig. 8 a and b. In addition, Fig. 8c shows that when the tension in the specimen finally is removed after the fracture, the opened cracks close again. This shows that opening of interlamellar cracks or pores or poorly adhered areas between well adhering contact points causes the non-linear elastic behaviour observed in the tensile test. No significant crack opening is observed in Fig. 9a and b in NiCrBSi HVAF H coating and hence no non-linear elastic behaviour in the tensile test. In this sense, the coating is more intact because it lacks the sufficiently long, continuous, openable defect structures found in APS and HVOF coatings. On the other hand, however, HVAF coatings have a relatively low fracture strength, which in this case is most likely due to the presence of unfused particles. For HVAF coatings it may therefore be better to use a slightly finer particle size distribution.

3.4. Cavitation erosion

In the cavitation erosion test, the wear mechanism is based on crack growth and fragmentation. Therefore, it could be thought to be a good measure of lamellar adhesion. Cavitation erosion results are shown in Fig. 10 a as well as in Table 3. Fig. 11 a shows the cavitation erosion resistance as a function of $\Delta\sigma/\Delta L$ and Fig. 11 b as a function of hardness. Results show that the spraying process has a significant effect on cavitation resistance. In contrast, the large difference in hardness of the coatings does not appear to have a significant effect on the cavitation erosion resistance of the coatings. Since cavitation proceeds through crack growth, which occurs mainly along lamellar boundaries, it is likely that the quality of lamellar cohesion and the oxides at the lamellar boundaries in the coating are important factors in the resistance to cavitation erosion.

Also high compressive stresses in thermally sprayed WC-CoCr coatings have been found to hinder crack propagation and improve their cavitation resistance [40]. For these coatings, the residual stresses shown in Table 3 do not appear to play as significant role in cavitation erosion resistance than the quality of lamella boundaries. Among the coatings studied, the deposition stresses are highest in NiCr HVOF and HVAF coatings, where compressive deposition stresses may have an impact on their good cavitation resistance. However, the cavitation erosion resistance of these coatings was worse than that of HVAF NiCrBSi, highlighting the importance of good structural integrity. It should be noted that in addition to the deposition stresses, the coatings are also subject to CTE mismatch stresses during cooling. From the changes in the curvature of the coating materials during the cooling phase, it was found that the CTEs in this case are only slightly higher than the thermal expansion coefficient of the coating ($12 * 10^{-6}$ 1/°C). Thus, CTE mismatch stresses add a tensile stress to the coating with a relatively small effect, estimated at 50–100 MPa. However, the compressive stresses due to CTE mismatches in the coatings are so low that their effect can be estimated to be marginal.

Plotting the cavitation erosion resistance as a function of the $\Delta\sigma/\Delta L$ of the stress-strain curve illustrates the dependence of these results in Fig. 11a. This interaction appears to be such that coatings with low $\Delta\sigma/\Delta L$ resist cavitation moor poorly than coatings with higher $\Delta\sigma/\Delta L$. It can be argued that dg/dL is a good indicator of coating integrity and good cavitation erosion resistance. As the integrity of the coating improves, improving cavitation resistance becomes more difficult and the coating material approaches its maximum achievable level. This maximum level can therefore be thought to be such that the density of defects such as porosity and oxides in the coating is low enough that they do not dominate its cavitation erosion resistance. The hardness of the coating can also be taken as some indication of the integrity of thermally sprayed coatings. Improved coating cohesion typically results in higher hardness, and improves the cavitation resistance as shown in Fig. 11 b. However, conventional hardness measurement typically results in a single constant load result, and thus the stress-strain dependence of the coating cannot be examined. The hardness measurement is also performed on the compression side; thus, the lamellae interfaces cannot easily open as is the case in tensile test. In addition, in the case of NiCr-based coatings, hardness measurement shows that oxidation increases the hardness even if its effect on interlamellar cohesion is negative.

NiCrBSi-H coating, which had the highest number of non-melted

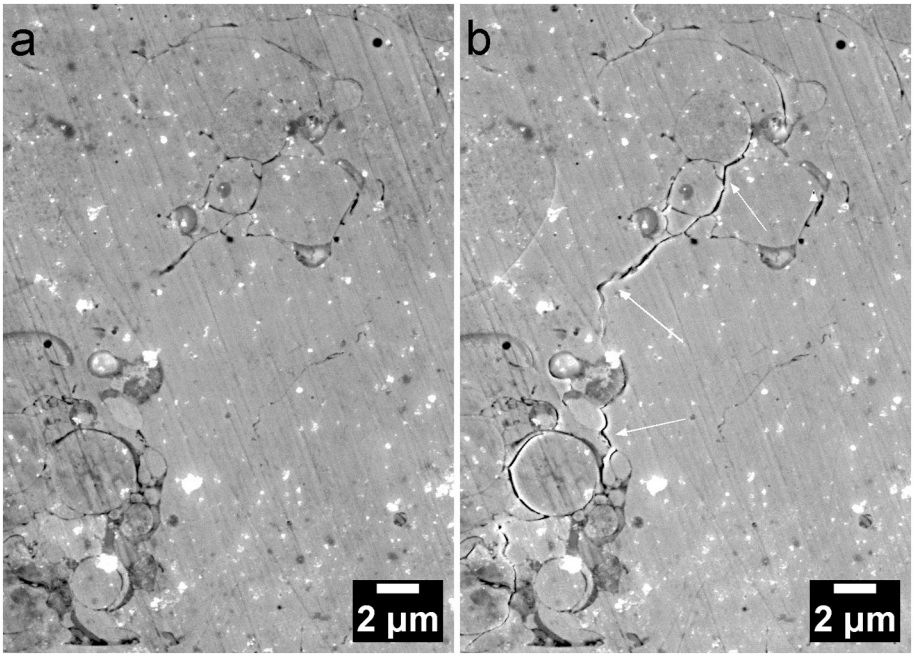

Fig. 7. In-situ SEM images on the NiCrBSi APS specimen surface during the tensile testing. a) On the left specimen surface before loading and b) on the right white arrows showing grown cracks on the surface of the specimen after approximately 0,094 mm displacement.

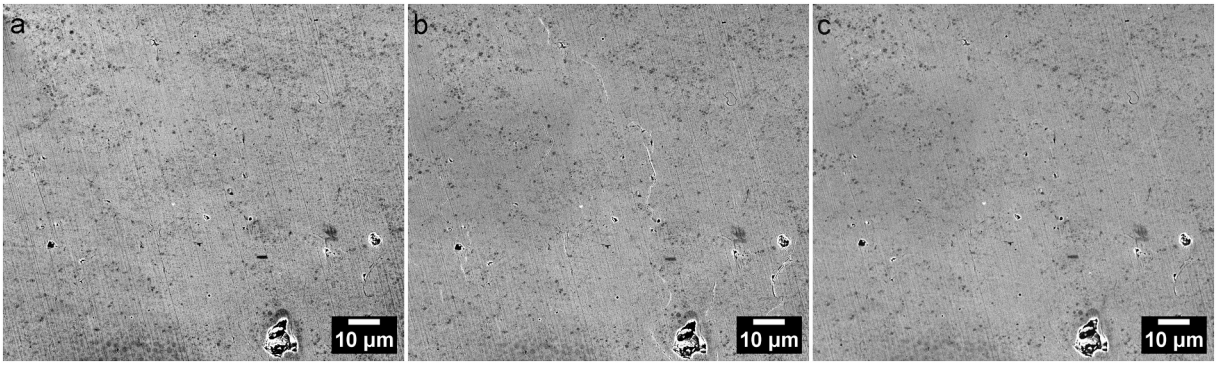

Fig. 8. SEM images of the NiCrBSi HVOF C specimen surface taken during the tensile test showing a) specimen surface before loading and b) cracks on the specimen surface after 0.11 mm displacement and c) closed cracks after stress release due to specimen fracture.

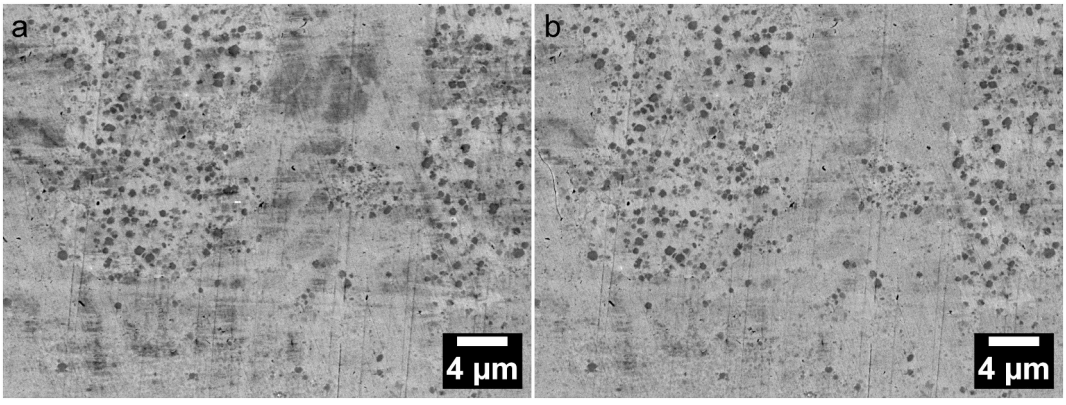

Fig. 9. SEM images of the NiCrBSi HVAF H specimen surface taken during the tensile test showing a) specimen surface before loading and b) specimen surface after 0.022 mm displacement.

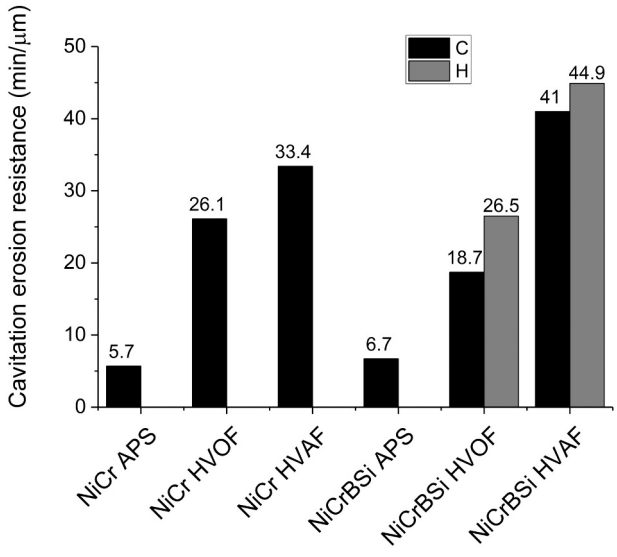

Fig. 10. Cavitation erosion resistances of the coatings.

particles at the fracture surface, had the best cavitation resistance. Presumably for this reason its UTS was relatively low. This is a surprising result, as it is often thought that poor lamellar adhesion affects the ease of propagation of cavitation cracks. However, in this study the non-melted particles do not adversely affect the cavitation resistance, even if their cohesion proved to be the weak link in the coating. Overall, the UTS did not seem to correlate with cavitation erosion resistance. This phenomenon was not well understood in this study.

4. Conclusions

In this study, a miniature tensile test was performed on free-standing APS, HVOF and HVAF sprayed NiCr and NiCrBSi coatings to obtain not only the stress displacement curve for the coatings but also the fracture strength of the coatings. A cavitation test was also performed on the coatings, which was thought to be a sensitive test to indicate the quality of the lamellar boundaries of the coatings. The tensile testing of the coatings provided useful information on the mechanical behaviour of HVAF, HVOF and APS coatings with the following conclusions:

- A non-linear stress-displacement curve was observed for all tested NiCr and NiCrBSi coatings. The amount of nonlinearity of the coatings sprayed by different methods varied. When the slope of the stress-displacement curve ($\Delta\sigma/\Delta L$ indicating the elastic modulus) was determined just before fracture, it was found that the $\Delta\sigma/\Delta L$ of HVAF coatings was higher than that of HVOF coatings, which was higher than that of APS coatings. This indicates the integrity of the coating structure.
- The final fracture of the coatings was found to occur particularly easily along the interfaces of the non-melted particles in the coatings and was in this respect dependent on the total cohesive area at the fracture surface. However, UTS was not a very good indicator of lamellar cohesion in this study, as all coatings had a high number of random defects related to sample manufacturing or inherent voids especially non-melted particles, that dominated the fracture process of the coating.

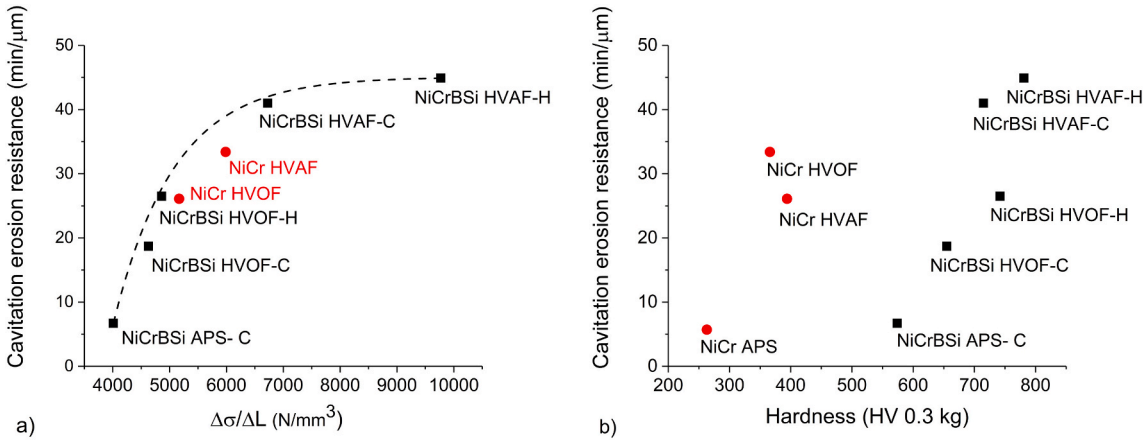

Fig. 11. a) cavitation erosion resistance as a function of Δσ/ΔL (slope of the stress-displacement curve) amd b) cavitation erosion resistance as a function of hadness.

– Cavitation resistance was best for HVAF coatings with the highest Δσ/ΔL, indicating good integrity of the coating. Also, for the other coatings, the degree of non-linearity of the tensile stress-displacement curve Δσ/ΔL gave a very good indication of their resistance to cavitation erosion.

CRediT authorship contrribution statement

Tommi Varis: Investigation, Conceptualization, Methodology, Visualization, Writing- Original draft preparation, Reviewing and Editing.

Aki Mäkelä: Investigation, Conceptualization, Methodology, Visualization, Writing- Original draft preparation.

Tomi Suhonen: Investigation, Conceptualization, Writing-Reviewing.

Jussi Laurila: Investigation, Writing- Reviewing.

Petri Vuoristo: Supervision.

Declaration of competing interest

The authors declare that they have no known competing financial interests or personal relationships that could have appeared to influence the work reported in this paper.

Data availability

Data will be made available on request.

Acknowledgements

The research was funded by Academy of Finland, project “Enabling phenomena behind multihierarchical strengthening of high kinetic sprayed metallic coatings” (HIERARCH, Decision NUM: 318064). Authors would like to thank Anssi Metsähonkala and Jarkko Lehti from Tampere University, Thermal Spray Center Finland (TSCF), Tampere, Finland, for spraying the coatings and Jorma Vihinen from Tampere University, Tampere, Finland, for laser cutting the specimens. We would also like to thank Asta Nurmela and Vilma Ratia from VTT for their work in conducting the miniature tensile testing.

References

[1] P. Vuoristo, Comprehensive Materials Processing, Elsevier Ltd, 2014.
[2] F. Fanicchia, X. Maeder, J. Ast, A.A. Taylor, Y. Guo, M.N. Polyakov, J. Michler, D. A. Axinte, Residual stress and adhesion of thermal spray coatings: microscopic view by solidification and crystallisation analysis in the epitaxial CoNiCrAlY single splat, Mater. Des. 153 (2018) 36–46, https://doi.org/10.1016/j.matdes.2018.04.040.
[3] E.E. Balić, M. Hadad, P.P. Bandyopadhyay, J. Michler, Fundamentals of adhesion of thermal spray coatings: adhesion of single splats, Acta Mater. 57 (2009) 5921–5926, https://doi.org/10.1016/j.actamat.2009.08.042.
[4] R. McPherson, B. Schafer, Interlamellar contact within plasma-spreyed coatings, Thin Solid Films 97 (1982) 201–204.
[5] R. Nieminen, P. Vuoristo, K. Niemi, T. Mäntylä, G. Barbezat, Rolling contact fatigue failure mechanisms in plasma and HVOF sprayed WC-Co coatings, Wear (1997), https://doi.org/10.1016/S0043-1648(97)00138-5.
[6] A. Vackel, T. Nakamura, S. Sampath, Mechanical behavior of spray-coated metallic laminates, J. Therm. Spray Technol. 25 (2016) 1009–1019, https://doi.org/10.1007/s11666-016-0404-x.
[7] S.H. Leigh, C.K. Lin, C.C. Berndt, Elastic response of thermal spray deposits under indentation tests, J. Am. Ceram. Soc. 80 (1997) 2093–2099, https://doi.org/10.1111/j.1151-2916.1997.tb03093.x.
[8] L. Chen, G.J. Yang, C.X. Li, C.J. Li, Hierarchical formation of intrasplat cracks in thermal spray ceramic coatings, J. Therm. Spray Technol. 25 (2016) 959–970, https://doi.org/10.1007/s11666-016-0420-x.
[9] A. Valarezo, W.B. Choi, W. Chi, A. Gouldstone, S. Sampath, Process control and characterization of NiCr coatings by HVOF-DJ2700 system: a process map approach, J. Therm. Spray Technol. 19 (2010) 852–865, https://doi.org/10.1007/s11666-010-9492-1.
[10] A.S.M. Ang, C.C. Berndt, A review of testing methods for thermal spray coatings, Int. Mater. Rev. 59 (2014) 179–223, https://doi.org/10.1179/1743280414Y.0000000029.
[11] C. Li, A. Ohmori, R. Mcpherson, The relationship between microstructure and Young's modulus of thermally sprayed ceramic coatings, J. Mater. Sci. 32 (1997) 997–1004, https://doi.org/10.1023/A:1018574221589.
[12] S.H. Leigh, G.C. Lee, C.C. Berndt, Modelling of elastic constants of plasma spray deposits with spheroid-shaped voids, Proc. Int. Therm. Spray Conf. 1 (1998) 587–592, https://doi.org/10.31399/asm.cp.itsc1998p0587.
[13] K. Tani, H. Nakahira, K. Miyajima, Y. Harada, in: Tani 1992 Thermal and Elastic Anisotropy of Thermally Sprayed Coatings.pdf 33, 1992, pp. 618–626.
[14] L. Pawlowski, The Science and Engineering of Thermal Spray Coatings, Second Edition, John Wiley and Sons, 2008, https://doi.org/10.1002/9780470754085.
[15] Y. Tan, A. Shyam, W.B. Choi, E. Lara-Curzio, S. Sampath, Anisotropic elastic properties of thermal spray coatings determined via resonant ultrasound spectroscopy, Acta Mater. 58 (2010) 5305–5315, https://doi.org/10.1016/j.actamat.2010.06.003.
[16] R.S. Lima, S.E. Kruger, B.R. Marple, Towards engineering isotropic behaviour of mechanical properties in thermally sprayed ceramic coatings, Surf. Coat.Technol. 202 (2008) 3643–3652, https://doi.org/10.1016/j.surfcoat.2008.01.005.
[17] N. Margadant, J. Neuenschwander, S. Stauss, H. Kaps, A. Kulkarni, J. Matejicek, G. Rössler, Impact of probing volume from different mechanical measurement methods on elastic properties of thermally sprayed Ni-based coatings on a mesoscopic scale, Surf. Coat.Technol. 200 (2006) 2805–2820, https://doi.org/10.1016/j.surfcoat.2005.02.201.
[18] T. Wakui, J. Malzbender, R.W. Steinbrech, Strain analysis of plasma sprayed thermal barrier coatings under mechanical stress, J. Therm. Spray Technol. 13 (2004) 390–395, https://doi.org/10.1361/10599630420425.
[19] S. Kuroda, T.W. Clyne, The quenching stress in thermally sprayed coatings, Thin Solid Films 200 (1991) 49–66, https://doi.org/10.1016/0040-6090(91)90029-W.
[20] Y. Liu, T. Nakamura, G. Dwivedi, A. Valarezo, S. Sampath, Anelastic behavior of plasma-sprayed zirconia coatings, J. Am. Ceram. Soc. 91 (2008) 4036–4043, https://doi.org/10.1111/j.1551-2916.2008.02789.x.
[21] G. Dwivedi, T. Nakamura, S. Sampath, Controlled introduction of anelasticity in plasma-sprayed ceramics, J. Am. Ceram. Soc. 94 (2011) s104–s111, https://doi.org/10.1111/j.1551-2916.2011.04494.x.
[22] M. Gupta, A. Weber, N. Markocsan, M. Gindrat, Electrochemical performance of plasma sprayed metal supported planar solid oxide fuel cells, J. Electrochem. Soc. 163 (2016) F1059–F1065, https://doi.org/10.1149/2.0791609jes.

[23] Y. Liu, T. Nakamura, V. Srinivasan, A. Vaidya, A. Gouldstone, S. Sampath, Non-linear elastic properties of plasma-sprayed zirconia coatings and associated relationships with processing conditions, Acta Mater. 55 (2007) 4667–4678, https://doi.org/10.1016/j.actamat.2007.04.037.
[24] T. Varis, E. Rajamäki, K. Korpiola, Mechanical properties of thermal spray coatings, in: C. Berndt, K. Khor, E. Lugscheider (Eds.), Therm. Spray 2001 New Surfaces a Millenium, ASM International, Materials Park, OH, USA, 2001, pp. 993–997.
[25] D. Hathiramani, R. Vaßen, D. Stöver, R.J. Damani, Comparison of atmospheric plasma sprayed anode layers for SOFCs using different feedstock, Proc. Int. Therm. Spray Conf. 15 (2006) 593–597, https://doi.org/10.1361/105996306X146811.
[26] C. Lin, S. Leigh, in: Free-Standing Forms During Four-Point Bend Tests 94, 1997, pp. 2382–2394.
[27] https://mymetco.oerlikon.com/en-us/article/1000787, (n.d.).
[28] https://mymetco.oerlikon.com/en-us/category/metco43vfns, (n.d.).
[29] M. Oksa, J. Metsäjoki, Optimizing NiCr and FeCr HVOF coating structures for high temperature corrosion protection applications, J. Therm. Spray Technol. 24 (2015) 436–453, https://doi.org/10.1007/s11666-014-0192-0.
[30] M. Somervuori, T. Varis, M. Oksa, T. Suhonen, P. Vuoristo, Comparative study on the corrosion performance of APS-, HVOF-, and HVAF-sprayed NiCr and NiCrBSi coatings in NaCl solutions, J. Therm. Spray Technol. 31 (2022) 1581–1597, https://doi.org/10.1007/s11666-022-01389-x.
[31] E. Sadeghimeresht, N. Markocsan, P. Nylén, A comparative study on Ni-based coatings prepared by HVAF, HVOF, and APS methods for corrosion protection applications, J. Therm. Spray Technol. 25 (2016) 1604–1616, https://doi.org/10.1007/s11666-016-0474-9.
[32] J. Matejicek, S. Sampath, D. Gilmore, R. Neiser, In situ measurement of residual stresses and elastic moduli in thermal sprayed coatings part 2: processing effects on properties of Mo coatings, Acta Mater. 51 (2003) 873–885, https://doi.org/10.1016/S1359-6454(02)00477-9.
[33] G.G. Stoney, The tension of metallic films deposited by electrolysis, Proc. R. Soc. A Math. Phys.Eng. Sci. 82 (1909) 172–175, https://doi.org/10.1098/rspa.1909.0021.
[34] A. Mäkelä, A Study on Interlamellar Cohesion Strength Estimation in Thermally Sprayed Coatings, Tampere University, 2020.
[35] M. Oksa, T. Varis, T. Suhonen, M. Jokipii, Optimising NiCr thermal spray coating with process map methodology for high temperature power plant boiler application, in: Int. Therm. Spray Conf. ITSC, Houston, ASM International, 2012.
[36] Š. Houdková, E. Smazalová, M. Vost, J. Schubert, Properties of NiCrBSi coating, as sprayed and remelted by different technologies, Surf. Coat. Technol. 253 (2014) 14–26, https://doi.org/10.1016/j.surfcoat.2014.05.009.
[37] J.M. Miguel, J.M. Guilemany, S. Vizcaino, Tribological study of NiCrBSi coating obtained by different processes, Tribol. Int. 36 (2003) 181–187, https://doi.org/10.1016/S0301-679X(02)00144-5.
[38] N. Ahmed, M.S. Bakare, D.G. McCartney, K.T. Voisey, The effects of microstructural features on the performance gap in corrosion resistance between bulk and HVOF sprayed Inconel 625, Surf. Coat.Technol. 204 (2010) 2294–2301, https://doi.org/10.1016/j.surfcoat.2009.12.028.
[39] V. T, K. K, J. P, A. P, Tensile testing of HVOF-sprayed coatings, in: Therm. Spray 1999 United Therm. Spray Conf, 1999.
[40] T. Varis, T. Suhonen, J. Laakso, M. Jokipii, P. Vuoristo, Evaluation of residual stresses and their influence on cavitation erosion resistance of high kinetic HVOF and HVAF-sprayed WC-CoCr coatings, J. Therm. Spray Technol. 29 (2020) 1365–1381, https://doi.org/10.1007/s11666-020-01037-2.